Applied Physics
Express

LETTER • **OPEN ACCESS**

Physical reservoir computing with graphene-based solid electric double layer transistor and the information processing capacity analysis

To cite this article: Hina Kitano *et al* 2025 *Appl. Phys. Express* **18** 024501

Applied Physics Express **18**, 024501 (2025) LETTER
https://doi.org/10.35848/1882-0786/adb19b

Physical reservoir computing with graphene-based solid electric double layer transistor and the information processing capacity analysis

Hina Kitano[1,2], Daiki Nishioka[1,3], Kazuya Terabe[1], and Takashi Tsuchiya[1,2*]

[1]Research Center for Materials Nanoarchitectonics (MANA), National Institute for Materials Science (NIMS), 1-1 Namiki, Tsukuba, Ibaraki 305-0044, Japan
[2]Department of Applied Physics, Faculty of Advanced Engineering, Tokyo University of Science, Katsushika, Tokyo 125-8585, Japan
[3]International Center for Young Scientists (ICYS), NIMS, 1-1 Namiki, Tsukuba, Ibaraki 305-0044, Japan

*E-mail: TSUCHIYA.Takashi@nims.go.jp

Received December 22, 2024; revised January 26, 2025; accepted February 2, 2025; published online February 13, 2025

Physical reservoir computing (PRC) is helpful for power reduction in machine learning technology, although the challenge is to improve computational performance. In this study, we developed a PRC device utilizing ion-electron coupled dynamics in an electric double layer transistor (EDLT) consisting of monolayer graphene channels and a Li^+ conducting inorganic oxide thin film. The ambipolar transfer characteristics of graphene channels in the EDLT obtained complex and diverse drain current responses, providing high information processing capacity and high PRC performance in the nonlinear autoregressive moving average (NARMA) task. © 2025 The Author(s). Published on behalf of The Japan Society of Applied Physics by IOP Publishing Ltd

Supplementary material for this article is available online

Recently, the research and development of brain-inspired computing, or neuromorphic computing, has been progressing in order to reduce the power consumption of machine learning, which has been increasing exponentially with the advent of deep learning and generative AI in the past decade.1) In particular, physical reservoir computing (PRC), which uses the nonlinear phenomena exhibited by physical devices as dynamical systems to perform information processing, has been attracting attention,2) and material-based PRC or *in-materio* reservoir computing, which uses the nonlinear phenomena that occur inside materials, is particularly promising due to its excellent versatility.3–17) For example, Usami et al. showed that it is possible to solve short-term memory tasks and speech recognition tasks with high accuracy using the electrical response of the organic electrochemical network formed by sulfonated polyaniline, strongly suggesting that the intrinsic properties of materials can be used as computational resources.4) Many researchers have been working on exploring various material systems for application to PRC, such as soft bodies, atomic switches, nanowire networks, ferroelectrics, and spintronics materials, and the movement is showing remarkable development.3–17) The present authors reported that the interaction between ion and electron transport in electric double layer transistors (EDLTs) fabricated using ion-conducting inorganic oxide thin films and hydrogen-terminated diamond single crystals produced complex electrical responses and that it was possible to perform various time series data processing.18–21) However, unlike simulation-based machine learning, which can freely set hyperparameters and optimize performance, the correlation between the properties of the EDLTs and the computation performance, and the degree of this correlation were unclear, making it challenging to obtain design guidelines for achieving higher performance.

In this study, we developed an EDLT consisting of graphene and a lithium ion-conducting inorganic solid electrolyte thin film and evaluated its physical reservoir computing performance. Graphene has a Dirac cone-type electronic structure, and is a semi-metal that exhibits both n-type and p-type ambipolar transport by controlling the Fermi level.22) Its *I-V* characteristics differ significantly from those of the hydrogen-terminated diamond, which was used in the previous reports and is a wide-gap semiconductor,18–21) so it is possible to investigate how the *I-V* characteristics of the channel material affect the computation performance. In addition to the nonlinear autoregressive moving-average (NARMA) task, which is a typical benchmark task for PRC,17,18,21,23–26) we analyzed the information processing capacity (IPC), which is an index of computation performance that is independent of the type of task, for the evaluation of PRC performance.27–29) By controlling the voltage width and pulse period of the gate voltage pulse streams used for information input as hyperparameters and evaluating them, we investigated how the *I-V* characteristics of the EDLT correlate with computation performance to obtain guidelines for improving the performance of the PRC device.

Figure 1(a) shows the schematic of the fabricated EDLT consisting of a Li^+ conducting amorphous oxide thin film and monolayer graphene. A chemical vapor deposition (CVD) grown monolayer graphene on SiO_2/Si substrate was used as the channel. Au/Cr thin films were deposited as source and drain electrodes using photolithography and electron-beam evaporation. Li^+ conducting amorphous Li-Nb-O (*a*-LN) and Li^+-hole mixed conducting $LiCoO_2$ thin films were then deposited by pulsed laser deposition. Pt was also deposited on top of the $LiCoO_2$ layer as a current collector [Fig. 1(b)]. The number of graphene layers was confirmed to be one from the Raman spectrum of the channel, consisting of G band ($1582\,cm^{-1}$) and D band ($2685\,cm^{-1}$) [Fig. 1(b) inset].30) Six channels with different channel lengths (channel length: $5 \sim 100\,\mu m$) were fabricated to obtain diverse output from the EDLT, as shown in an optical microscopy image of the actual graphene channels [Fig. 1(c)]. Please refer to the supplementary information for

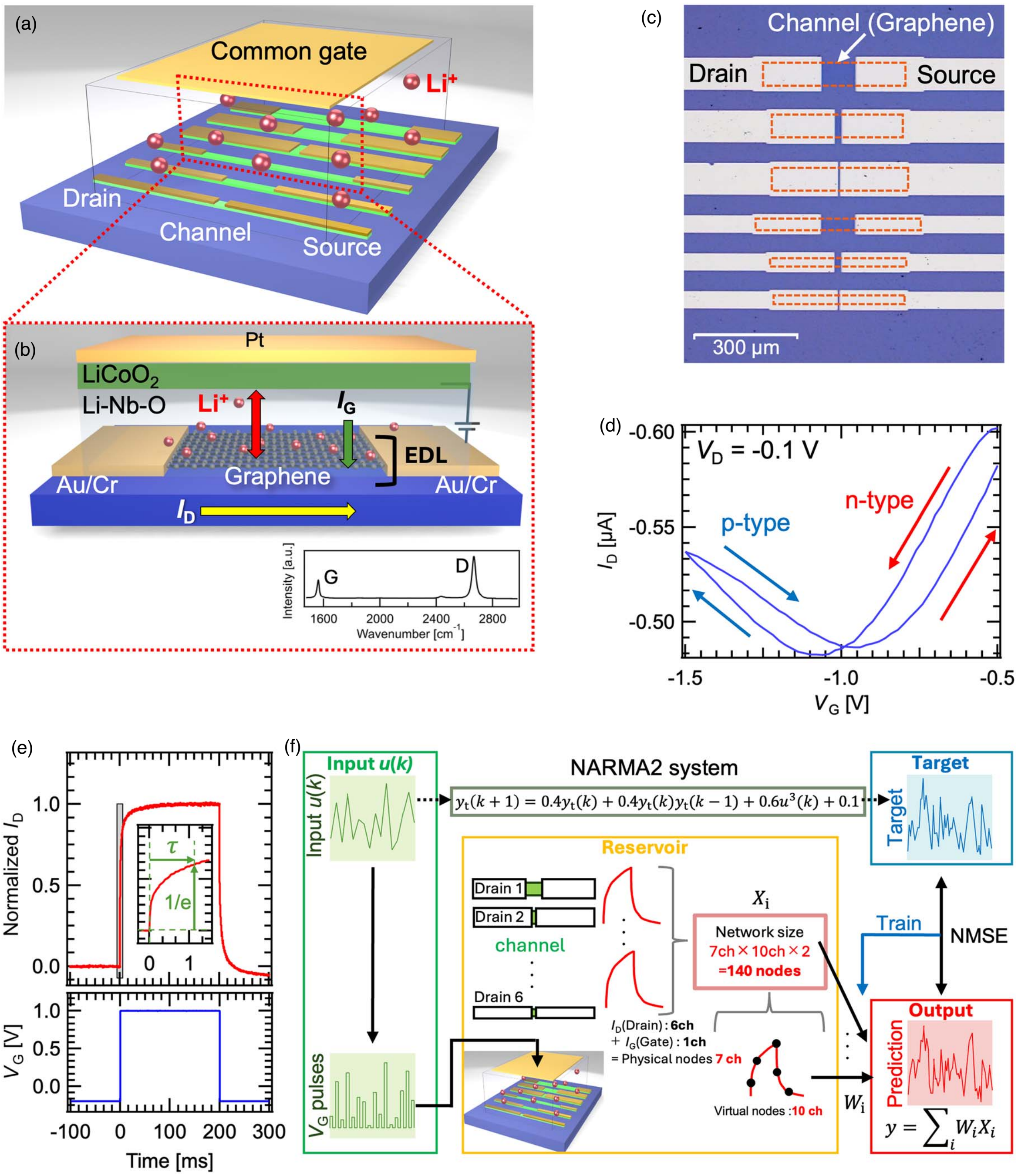

Fig. 1. (a) Schematic illustration of the EDL-based IGR consisting of graphene and *a*-LN. (b) Schematic of the EDL mechanism in the IGR. The inset shows the Raman spectrum of the graphene channel. (c) Optical microscope image of graphene channels. (d) The I_D -V_G characteristic of the EDLT. (e) A typical I_D response of the EDLT against V_G pulse. (f) Schematic of the NARMA2 task in the study.

details on device fabrication. Figure 1(d) shows the transfer curve of the EDLT for a channel length of 100 mm, measured at a drain voltage (V_D) of -0.1 V. As positive gate voltage (V_G) is applied to the EDLT, Li$^+$ ions move towards the channel side and electrons accumulate in the graphene channel (an EDL charging), reducing the channel resistance and increasing drain current (I_D), and vice versa. The ambipolar (V-shaped) transfer characteristic observed in Fig. 1(d) is a typical behavior of the graphene-based field effect transistors.[22,31–34] It corresponds to the Dirac-cone-like band structure of the monolayer graphene. The hysteresis observed in the transfer curve is due to the relatively slow relaxation of Li$^+$ near the *a*-LN/graphene interface, which is beneficial for enhancing short-term memory. Figure 1(e) shows a typical I_D response of the EDLT against a single V_G pulse. From the I_D response, the time constant (τ) of the EDL charging/discharging is derived to be approximately 1.10 ms by assuming the condition, where, at $t = \tau$, I_D reduces to 1/e of the initial value A [i.e., 37% of A (decrement is 63% of A)].[19]

Such I_D responses of the EDLT were utilized as computation resources in the PRC scheme, as shown in Fig. 1(f). Its performance was evaluated based on a second-order nonlinear autoregressive moving-average (NARMA2) task, a typical benchmark task for PRCs (details of the task are discussed later). Time-series data $u(k)$ is inputted in the input layer, where k is the time step. In the present case, $u(k)$ is input as V_G pulse streams. Subsequently, $u(k)$ is mapped into

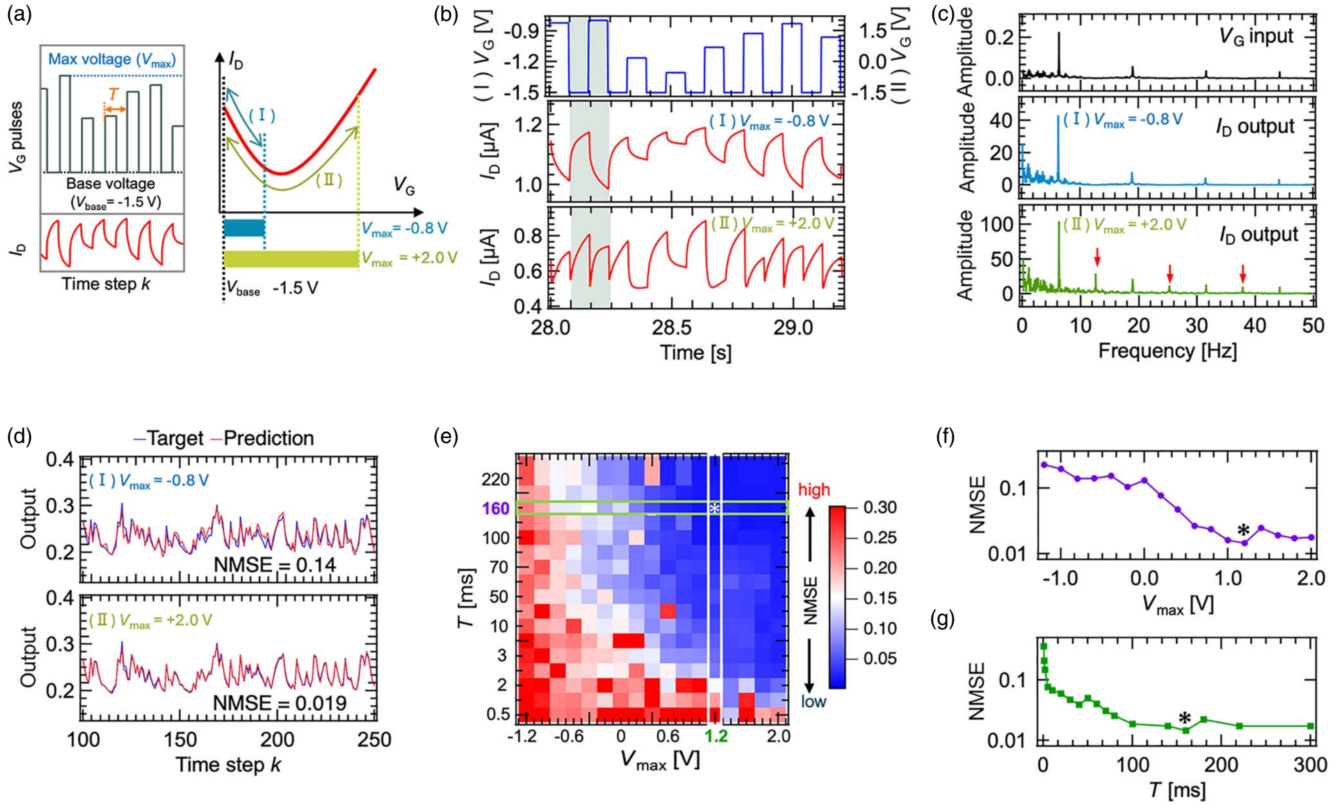

Fig. 2. (a) Relationship between V_G parameters (V_{max}, V_{base}) and the corresponding I_D response. (b) I_D responses under the two V_{max} conditions [(I) and (II)]. (c) The fast Fourier transform (FFT) spectrum of (I) and (II). (d) The target and prediction waveforms under conditions (I) and (II). (e) The pulse period T and V_{max} dependence of NMSEs. The optimal condition is indicated by *. (f) NMSE dependence on V_{max} ($T = 160$ ms). (g) NMSE dependence on T ($V_{max} = +1.2$ V).

a nonlinear high-dimensional space through the ion-electron coupling dynamics within the EDLT serving as the reservoir layer. These are represented as various I_D responses (spatial state evolution) and time-multiplexing (temporal state evolution), yielding the reservoir state $X_i(k)$ at each node i ($i = 1, 2, \ldots, N$). The reservoir output $y(k)$ is obtained as a linear combination of $X_i(k)$ and the readout weights w_i, as follows,

$$y(k) = \sum_{i=1}^{N} w_i X_i(k) + b \tag{1}$$

where N and b are the numbers of the reservoir state and bias, respectively. The readout weights were trained using ridge regression. The primary role of the EDLT as a physical reservoir, as mentioned above, is to serve as a mapping function into a high-dimensional space for the input. Therefore, the nonlinearity of the device's transfer curve significantly affects this mapping, while the I_D relaxation behavior strongly influences the effectiveness of the time-multiplexing method, namely, the high-dimensionality of the reservoir.

As mentioned above, we investigated the effect of the graphene's I_D-V_G characteristics on the information processing performance using the NARMA2 task, that predicts the NARMA2 model shown in Eq. (2).[35)]

$$\begin{aligned} y_t(k+1) &= 0.4 y_t(k) \\ &\quad + 0.4 y_t(k) y_t(k-1) + 0.6 u^3(k) + 0.1 \end{aligned} \tag{2}$$

Here, $u(k)$ is a random sequence with a uniform distribution taking values between 0 and 0.5. Equation (2) describes the state evolution y_t of the NARMA2 model, where the model output consists of terms such as cross-products of its own output with a two-step time lag and cubic terms of past inputs. Therefore, to accurately reproduce the NARMA2 model using the on-gating reservoir (IGR), the IGR must possess sufficient expressive power (i.e., nonlinearity and memory capacity) to represent these elements. As shown in Fig. 2(a), the input data was converted into a V_G pulse stream in the V_G range between the base V_G (V_{base}), which was fixed to -1.5 V, and the maximum V_G (V_{max}), which was varied from -1.2 to $+2.0$ V in each case. By varying V_{max}, the impact of the I_D-V_G characteristics of graphene on I_D responses and computational performance was investigated. For instance, when $V_{max}=-0.8$ V (indicated by the blue arrow), it is below the Dirac point, resulting in a monotonic I_D-V_G characteristic and a simple I_D response. In contrast, when V_{max} exceeds the Dirac point (indicated by the green arrow), the I_D-V_G characteristic exhibits a V-shaped transfer curve, suggesting a more complex I_D response. To explore the relationship between I_D relaxation properties and computational performance, the pulse period T of the V_G pulse stream was set between 0.5 and 300 ms. The V_D were set to $+0.1$ V for all channels. To enhance the performance, we used the inverted input method.[20)] A V_G pulse stream was applied to the common gate, and the output current was measured from six drain terminals with different channel lengths and one gate terminal. In overall, there were a total of seven physical nodes: six I_D and one I_G. From each current waveform, 10 virtual nodes were extracted (time-multiplexing). Thus, under $N = 140$, the reservoir output y was obtained as described in Eq. (1). The computational performance was evaluated using the normalized mean square error (NMSE) defined as follows:

$$\mathrm{NMSE} = \frac{1}{M}\frac{\sum_{k=1}^{M}[y_t(k) - y(k)]^2}{\sigma^2[y_t(k)]} \tag{3}$$

where M is the data length ($M = 2000$ for the training phase and M=700 for the test phase); $s^2(\cdot)$ is the variance.

Figure 2(b) compares the I_D responses of channel 3 (ch3) to V_G pulse streams for representative V_{max} values: (I) $V_{max} = -0.8$ V ($T = 160$ ms) and (II) $V_{max} = +2.0$ V ($T = 160$ ms). Please refer to Fig. S1 for the other representative results. Under the condition (I) with $V_{max} = -0.8$ V, I_D response to the V_G variation from one to another appears to be simple in which I_D monotonously increases or decreases during V_G is constant. However, under the condition (II) with $V_{max} = +2.0$ V, I_D shows a complex response in which the direction of I_D variation (increases or decreases) changes even during V_G is constant. This unique I_D transient behavior originates from including the Dirac point in the measured V_G range and the resultant switching between n- and p-conduction during the EDL charging. Such behavior generates quasi-second harmonic waves, as shown in Fig. S2, demonstrating the excellent nonlinearity of the device. Power spectra derived by the Fourier transform help obtain an intuitive distribution of the higher-order terms of nonlinearity.[4] Figure 2(c) shows the fast Fourier transform (FFT) spectra of the V_G input and the corresponding I_D output under conditions (I) and (II). All three FFT spectra include a strong peak at 6.29 Hz and odd harmonics, which are caused by the V_G input in the form of a square wave with a duty ratio of 50%. Whereas the spectrum for condition (I) is similar to the one for the V_G input, even harmonics (indicated by the red arrows) are prominent only in the spectrum for condition (II), which indicates that the inclusion of Dirac point in the V_G range enhances the higher-order terms of nonlinearity. Target and predicted waveforms for the conditions (I) and (II) are compared in Fig. 2(d). Under condition (I), the prediction error is relatively large (NMSE = 0.14), whereas under condition (II), the predicted waveform closely matches the target waveform, and the prediction error during the testing phase is nearly an order of magnitude lower compared to that of condition (I) (NMSE = 0.019). This result indicates that strong nonlinearity in the device's transport characteristics significantly enhances computational performance in PRC.

Figure 2(e) illustrates the dependence of NMSE on V_{max} and T during the testing phase. As indicated by the asterisk in the figure, the optimal condition was achieved at $V_{max} = +1.2$ V and $T = 160$ ms, with a general trend of improved performance as V_{max} and T increased. Figure 2(f) shows the V_{max} dependence of NMSE at $T = 160$ ms [highlighted by the white square in Fig. 2(e)]. The NMSE decreases with increasing V_{max} up to $+1.2$ V and saturates beyond this value, reflecting performance improvement due to enhanced nonlinearity. Figure 2(g) presents the T dependence of NMSE at $V_{max} = +1.2$ V [highlighted by the green square in Fig. 2(e)]. NMSE decreases with increasing T, saturating around $T = 100$ ms. The broad operational range with high performance from $T = 100$ ms to 300 ms is particularly advantageous for processing time-series data across various time scales. Moreover, as shown in Fig. 2(e), increasing V_{max} to around 2 V achieves high performance even in a high-speed region with $T = 2 \sim 3$ ms. This demonstrates the potential for optimizing operational speed by tuning V_{max}. These results highlight the wide operational range and tunability of the device, underscoring its suitability as an integrated edge AI device for processing diverse time-series data.

To elucidate the relationship between the device's operating conditions (V_{max}) and the key RC characteristics (nonlinearity and memory capacity), the information processing capacity (IPC) of the IGR was evaluated, linking the tunable nonlinearity under different operating conditions to the device's nonlinear mapping capability in information processing. IPC is an index of the reservoir's computational power independent of tasks, quantitatively characterizing the reservoir's short-term memory and nonlinearity. The IPC is calculated based on the accuracy of regression tasks, where the reservoir generates outputs for targets transformed by n-degree polynomials of the input (and its delays).[27–29] The total capacity C_{tot} is defined as the sum of the sub-capacities C_n for each degree n.

$$C_{tot} = \sum_n C_n \tag{4}$$

Generally, a reservoir with a high C_{tot} can perform well across various tasks, exhibiting high computational performance. We performed the IPC analysis with n up to nine in this study: C_1 is the linear component corresponding to short-term memory, and $C_2 \sim C_9$ are the nonlinear components. Figure 3(a) shows the V_{max} dependence of C_{tot} and NMSE. Whereas C_{tot} monotonically increases as V_{max} rises in a positive direction, NMSE falls up to V_{max} of $+1.2$ V and then saturates. Related to the behavior, the V_{max} dependence of the

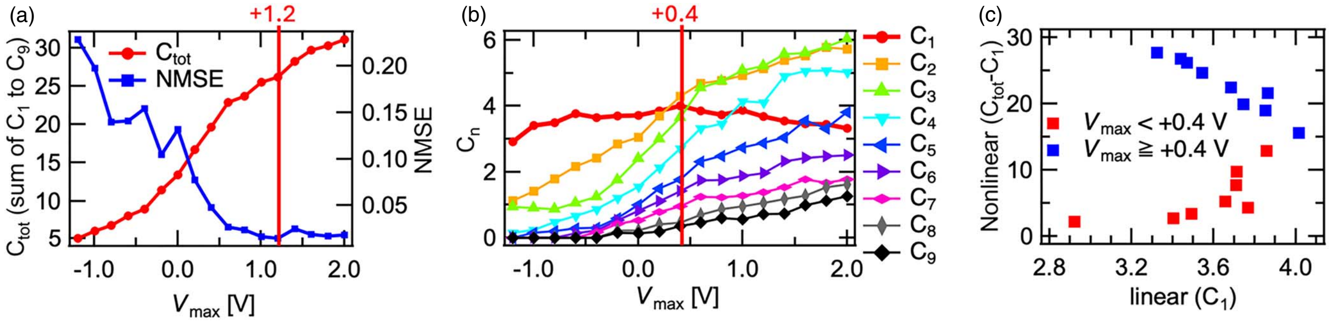

Fig. 3. (a) V_{max} dependence of C_{tot} and NMSE. (b) V_{max} dependence of IPC. (c) The relationship between the linear component (C_1) and the nonlinear component (C_{total}-C_1).

sub-capacities C_1 to C_9 in Fig. 3(b) includes contrasting tendencies for C_1 (linear component) and C_2 to C_9 (nonlinear components). While C_2 to C_9 monotonically increases with reference to V_{max}, C_1 peaks at $V_{\mathrm{max}} = +0.4\,\mathrm{V}$, indicating a trade-off relationship between C_1 and C_2 to C_9 in the high V_{max} region. Figure 3(c) shows the relationship between the linear component (C_1) and the nonlinear component (C_{total}-C_1), which are obtained with a variety of V_{max}. As expected from Fig. 3(b), the nonlinear component monotonically increases in the whole range, but the linear component peaks at $V_{\mathrm{max}} = +0.4\,\mathrm{V}$. Therefore, it was concluded that the decrease in C_1 (the short-term memory) above $V_{\mathrm{max}} = +0.4\,\mathrm{V}$ compensates for the benefit of the increase in the nonlinear component (C_{total}-C_1) and thus restricts the further improvement of computation performance. A similar trade-off relationship between linear and nonlinear components was observed in both theory and experiments.[36] The precise control of the relationship is thus of great importance in achieving high-performance PRC.

In this study, we developed PRC utilizing an EDLT-based IGR consisting of graphene and *a*-LN thin film and evaluated its PRC performance. Thanks to the ambipolar characteristic of graphene due to the Dirac cone-type electronic structure, which differs from previously reported diamond-based EDLT, the I_D-V_G characteristic takes V-shaped transfer curve. This provides complex and diverse I_D responses, which are under the strong influence of V_{max} and T, leading to the strong dependence of computation performance for the NARMA2 task on the parameters. By optimizing the operation condition, the lowest NMSE in the study was 0.015, which is 25% lower than the diamond-based EDL-IGR (NMSE = 0.020) in the previous report.[18] The computation performance dependence on V_{max} and T was further investigated by IPC analysis. While the nonlinear components C_2 to C_9 monotonically increase as the V_G range expands in a positive direction, the linear component C_1 peaks at $V_{\mathrm{max}} = +0.4\,\mathrm{V}$. The decrease in C_1 (i.e., the short-term memory) above $V_{\mathrm{max}} = +0.4\,\mathrm{V}$ compensates for the benefit of the increase in the nonlinear components (C_{total}-C_1, or C_2 to C_9), limiting the further improvement of computation performance. The result indicates that obtaining a high compatibility of linear and nonlinear IPC components in the output dynamics is vital for PRC devices. The optimization of hyperparameters, not only by the tuning of operation conditions of PRC devices, but also by the tuning of materials characteristics as dynamical systems based on materials science and technology can offer a reliable way to achieve high-performance PRC.

Acknowledgments This research was supported by the JFE 21st Century Foundation, JST PRESTO under Grant No. JPMJPR23H4, and JSPS KAKENHI under Grant No. JP24KJ0229 (Grant-in-Aid for JSPS Fellows). A part of this work was supported by ‘Advanced Research Infrastructure for Materials and Nanotechnology in Japan (ARIM)’ of the Ministry of Education, Culture, Sports, Science and Technology (MEXT) under Grant Nos. JPMXP1224NM5236 and JPMXP1224NM5357.

ORCID iDs Hina Kitano https://orcid.org/0009-0008-9132-0275
Daiki Nishioka https://orcid.org/0000-0002-3369-7700
Kazuya Terabe https://orcid.org/0000-0003-3988-3456
Takashi Tsuchiya https://orcid.org/0000-0002-6950-6160

---

1) D. Kramer, Phys. Today **77**, 28 (2024).
2) W. Maass, T. Natschläger, and H. Markram, Neural Comput. **14**, 2531 (2002).
3) H. Tanaka, M. Akai-Kasaya, A. TermehYousefi, L. Hong, L. Fu, H. Tamukoh, D. Tanaka, T. Asai, and T. Ogawa, Nat. Commun. **9**, 2693 (2018).
4) Y. Usami et al., Adv. Mater. **33**, 2102688 (2021).
5) Hadiyawarman, Y. Usami, T. Kotooka, S. Azhari, M. Eguchi, and H. Tanaka, Jpn. J. Appl. Phys. **60**, SCCF02 (2021).
6) H. O. Sillin, R. Aguilera, H. H. Shieh, A. V. Avizienis, M. Aono, A. Z. Stieg, and J. K. Gimzewski, Nanotechnology **24**, 384004 (2013).
7) M. Akai-Kasaya, Y. Takeshima, S. Kan, K. Nakajima, T. Oya, and T. Asai, Neuromorph. Comput. Eng. **2**, 014003 (2022).
8) S. Kan, K. Nakajima, T. Asai, and M. Akai-Kasaya, Adv. Sci. **9**, 2104076 (2022).
9) S. G. Koh, H. Shima, Y. Naitoh, H. Akinaga, and K. Kinoshita, Sci. Rep. **12**, 6958 (2022).
10) Y. Paquot, F. Duport, A. Smerieri, J. Dambre, B. Schrauwen, M. Haelterman, and S. Massar, Optoelectron. Reservo. Comput. Sci. Rep. **2**, 287 (2012).
11) K. Toprasertpong, E. Nako, Z. Wang, R. Nakane, M. Takenaka, and S. Takagi, Commun. Eng. **1**, 21 (2022).
12) S. Tsunegi, T. Taniguchi, K. Nakajima, S. Miwa, K. Yakushiji, A. Fukushima, S. Yuasa, and H. Kubota, Appl. Phys. Lett. **114**, 164101 (2019).
13) R. Nakane, G. Tanaka, and A. Hirose, IEEE Access **6**, 4462 (2018).
14) S. Lilak, W. Woods, K. Scharnhorst, C. Dunham, C. Teuscher, A. Z. Stieg, and J. K. Gimzewski, Front. Nanotechnol. **3**, 675792 (2021).
15) M. Nakajima, K. Minegishi, Y. Shimizu, Y. Usami, H. Tanaka, and T. Hasegawa, Nanoscale **14**, 7634 (2022).
16) Y. Shimizu, K. Minegishi, H. Tanaka, and T. Hasegawa, Jpn. J. Appl. Phys. **62**, SG1001 (2023).
17) K. Nakajima, H. Hauser, T. Li, and R. Pfeifer, Sci. Rep. **5**, 10487 (2015).
18) D. Nishioka, T. Tsuchiya, W. Namiki, M. Takayanagi, M. Imura, Y. Koide, T. Higuchi, and K. Terabe, Sci. Adv. **8**, eade1156 (2022).
19) M. Takayanagi, D. Nishioka, T. Tsuchiya, M. Imura, Y. Koide, T. Higuchi, and K. Terabe, Mater. Today Adv. **18**, 100393 (2023).
20) Y. Yamaguchi, D. Nishioka, W. Namiki, T. Tsuchiya, M. Imura, Y. Koide, T. Higuchi, and K. Terabe, Appl. Phys. Express **17**, 024501 (2024).
21) D. Nishioka, T. Tsuchiya, M. Imura, Y. Koide, T. Higuchi, and K. Terabe, Commun. Eng. **3**, 81 (2024).
22) A. K. Geim and K. S. Novoselov, Nat. Mater. **6**, 183 (2007).
23) T. Tsuchiya, D. Nishioka, W. Namiki, and K. Terabe, Adv. Electron. Mater. **10**, 2400625 (2024).
24) T. Wada, D. Nishioka, W. Namiki, T. Tsuchiya, T. Higuchi, and K. Terabe, Adv. Intell. Syst. **5**, 2300123 (2023).
25) K. Shibata, D. Nishioka, W. Namiki, T. Tsuchiya, T. Higuchi, and K. Terabe, Sci. Rep. **13**, 21060 (2023).
26) W. Namiki, D. Nishioka, Y. Yamaguchi, T. Tsuchiya, T. Higuchi, and K. Terabe, Adv. Intell. Syst. **5**, 2300228 (2023).
27) S. Tsunegi et al., Adv. Intell. Syst. **5**, 2300175 (2023).
28) J. Dambre, D. Verstraeten, B. Schrauwen, and S. Massar, Sci. Rep. **2**, 514 (2012).
29) N. Akashi, T. Yamaguchi, S. Tsunegi, T. Taniguchi, M. Nishida, R. Sakurai, Y. Wakao, and K. Nakajima, Phys. Rev. Res. **2**, 043303 (2020).
30) A. C. Ferrari et al., Phys. Rev. Lett. **97**, 187401 (2006).
31) F. Schwierz, Nat. Nanotech. **5**, 487 (2010).
32) A. Di Bartolomeo, F. Giubileo, S. Santandrea, F. Romeo, R. Citro, T. Schroeder, and G. Lupina, Nanotechnology **22**, 275702 (2011).
33) J. Wei, B. Liang, Q. Cao, H. Ren, Y. Zheng, and X. Ye, Carbon **156**, 67 (2020).
34) F. Urban, G. Lupina, A. Grillo, N. Martucciello, and A. Di Bartolomeo, Nano Express **1**, 010001 (2020).
35) A. F. Atiya and A. G. Parlos, IEEE Trans. Neural Networks **11**, 697 (2000).
36) M. Inubushi and K. Yoshimura, Sci. Rep. **7**, 10199 (2017).